

LETTER

Open Access



Arbitrarily structured quantum emission with a multifunctional metalens

Chi Li^{1,2*†}, Jaehyuck Jang^{3†}, Trevon Badloe^{4,5†}, Tieshan Yang¹, Joohoon Kim⁴, Jaekyung Kim⁴, Minh Nguyen¹, Stefan A. Maier^{2,6}, Junsuk Rho^{3,4,7,8*}, Haoran Ren^{2*}  and Igor Aharonovich^{1,9}

Abstract

Structuring light emission from single-photon emitters (SPEs) in multiple degrees of freedom is of great importance for quantum information processing towards higher dimensions. However, traditional control of emission from quantum light sources relies on the use of multiple bulky optical elements or nanostructured resonators with limited functionalities, constraining the potential of multi-dimensional tailoring. Here we introduce the use of an ultrathin polarisation-beam-splitting metalens for the arbitrary structuring of quantum emission at room temperature. Owing to the complete and independent polarisation and phase control at the single meta-atom level, the designed metalens enables simultaneous mapping of quantum emission from ultra-bright defects in hexagonal boron nitride and imprinting of an arbitrary wavefront onto orthogonal polarisation states of the sources. The hybrid quantum metalens enables simultaneous manipulation of multiple degrees of freedom of a quantum light source, including directionality, polarisation, and orbital angular momentum. This could unleash the full potential of solid-state SPEs for their use as high-dimensional quantum sources for advanced quantum photonic applications.

[†]These authors contributed equally to this work.

Chi Li, Jaehyuck Jang and Trevon Badloe are contributed equally to this work.

*Correspondence:

Chi Li

chi.li@uts.edu.au

Junsuk Rho

jsrho@postech.ac.kr

Haoran Ren

haoran.ren@monash.edu

¹ School of Mathematical and Physical Sciences, University of Technology Sydney, Ultimo, NSW 2007, Australia

² School of Physics and Astronomy, Monash University, Melbourne, VIC 3800, Australia

³ Department of Chemical Engineering, Pohang University of Science and Technology (POSTECH), Pohang 37673, Republic of Korea

⁴ Department of Mechanical Engineering, Pohang University of Science and Technology (POSTECH), Pohang 37673, Republic of Korea

⁵ Graduate School of Artificial Intelligence, Pohang University of Science and Technology (POSTECH), Pohang 37673, Republic of Korea

⁶ Department of Physics, Imperial College London, London SW7 2AZ, UK

⁷ POSCO-POSTECH-RIST Convergence Research Centre for Flat Optics and Metaphotonics, Pohang 37673, Republic of Korea

⁸ National Institute of Nanomaterials Technology (NINT), Pohang 37673, Republic of Korea

⁹ ARC Centre of Excellence for Transformative Meta-Optical Systems, University of Technology Sydney, Ultimo, NSW 2007, Australia

1 Introduction

Quantum emission is pivotal to the realisation of photonic quantum technologies, cryptography, communications, sensing, and computing [1, 2]. Solid-state single photon emitters (SPEs) such as defects in hexagonal boron nitride (hBN) operate at room temperature and are highly desired due to their robustness and brightness [3–5]. The conventional way to collect photons from SPEs often relies on a high numerical aperture (NA) objective lens or employing micro-structured antennas such as nanopillars [6]. While the efficiency of photon collection can be high, these tools lack the capability to manipulate quantum emission - particularly in regard to directionality or phase. Consequently, for achieving any desired structuring of the emitted quantum light source, multiple bulky optical elements such as polarisers and phase plates are inevitably required.

The ability to arbitrarily structure light in its multi-dimensions is of great importance for quantum light sources [7–13]. In this respect, metasurfaces have transformed the landscape of photonic design, propelling

major technological advances spanning from optical imaging [14, 15], displays [16], and holography [17–21], to LiDAR [22] and molecular sensing [23]. Recently, the direct integration of nanoscale emitters into nanostructured resonators and metasurfaces have been realised to collect [24, 25] and demonstrate basic tailoring of the SPEs emission [26–29]. These initial demonstrations, although with limited control over quantum emission, constituted the necessity for flat optics to advance the manipulation of quantum emission according to its multiple degrees of freedom.

Here we address this vision, by designing and engineering a multifunctional metalens, capable of tailoring the directionality, polarisation, and orbital angular momentum (OAM) degrees of freedom simultaneously (Fig. 1A). Specifically, we utilise the metalens to demonstrate a multidimensional structuring of quantum emission from SPEs in hBN, operating at room temperature. Since our designed meta-atoms in the metalens can achieve complete and independent polarisation and phase manipulation, it is possible to encode different wavefronts onto orthogonal polarisations of SPEs. Hence, we demonstrate arbitrary shaping of the directionality of quantum emission by adding phase gratings selective to orthogonal polarisations onto the metalens profile, which are represented by different spots in the momentum space

of the metalens (Fig. 1B). In addition, we show that different helical wavefronts can be further added onto the metalens profile, leading to the generation of distinctive OAM modes in orthogonal polarisations of SPEs, which are represented by doughnut-shaped spots with different sizes in momentum space (Fig. 1C). The demonstrated arbitrary wavefront shaping of quantum emission in multiple degrees of freedom could unleash the full potential of solid-state SPEs to be used as high-dimensional quantum sources for advanced quantum photonic applications.

2 Results

2.1 Design and fabrication of a multifunctional metalens

We design a polarisation beam-splitting metalens to decompose the emission from hBN into two orthogonal linear polarisation (LP) states along the x - and y -axis directions, denoted as LP $_x$ and LP $_y$, respectively. We chose the LP to match the linearly polarised emission profile of SPEs in hBN. However, we note that the design could be adapted for other orthogonal polarisations of light, such as left and right circularly polarised light. Taking advantage of the multiplexing possibility offered by the metalens, we add multiple functionalities—specifically controlling the directionality and polarisation, as well as structuring the OAM of quantum emission.

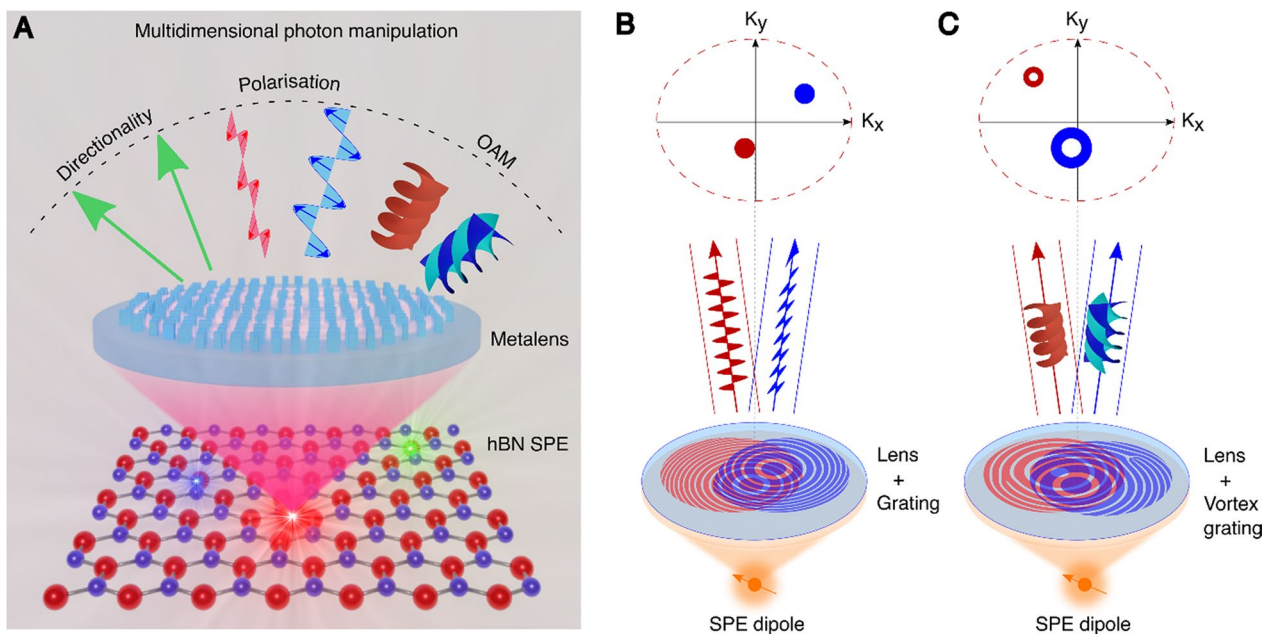


Fig. 1 Schematics of multidimensional manipulation of hBN quantum emission using a multifunctional metalens. **A** Directional photon splitting, polarisation control and subsequent OAM encoding. The green arrows stand for the directionality control of SPE emission collected by the metalens. The two sine waves indicate the splitting of SPE emission into two orthogonal polarised streams. The two helical beams indicate a further dressing by OAM. **B, C** Enlarged views of each encoding concept where grating and vortex grating are adapted to structure the photons in extra dimensions. In addition, the directionality of orthogonal linear polarisations is well inherited and projected as the red and blue spots in the momentum (k) space

To achieve this, we design cuboid shaped meta-atoms with a fixed height (H) and varying length (l), and width (d), arranged in a square lattice with periodicity (P), as shown in Fig. 2A. We choose low-loss hydrogenated amorphous silicon (a-Si:H) [30, 31] as the material of the metalens due to its negligible extinction coefficient in the visible emission of hBN SPEs (Additional file 1: Note S1). We assume that the meta-atoms act as truncated

rectangular waveguides, so with a sufficiently large H , any desired independent phase modulation (ϕ) to the incident LPx and LPy polarisation channels from $0-2\pi$ can be achieved by varying the transverse dimensions of l and d . Subsequently, we perform a parameter sweep of different values for H , l , and d , to design a meta-atom library for matching any required ϕ for LPx and LPy using an in-house-built rigorous coupled wave analysis (RCWA)

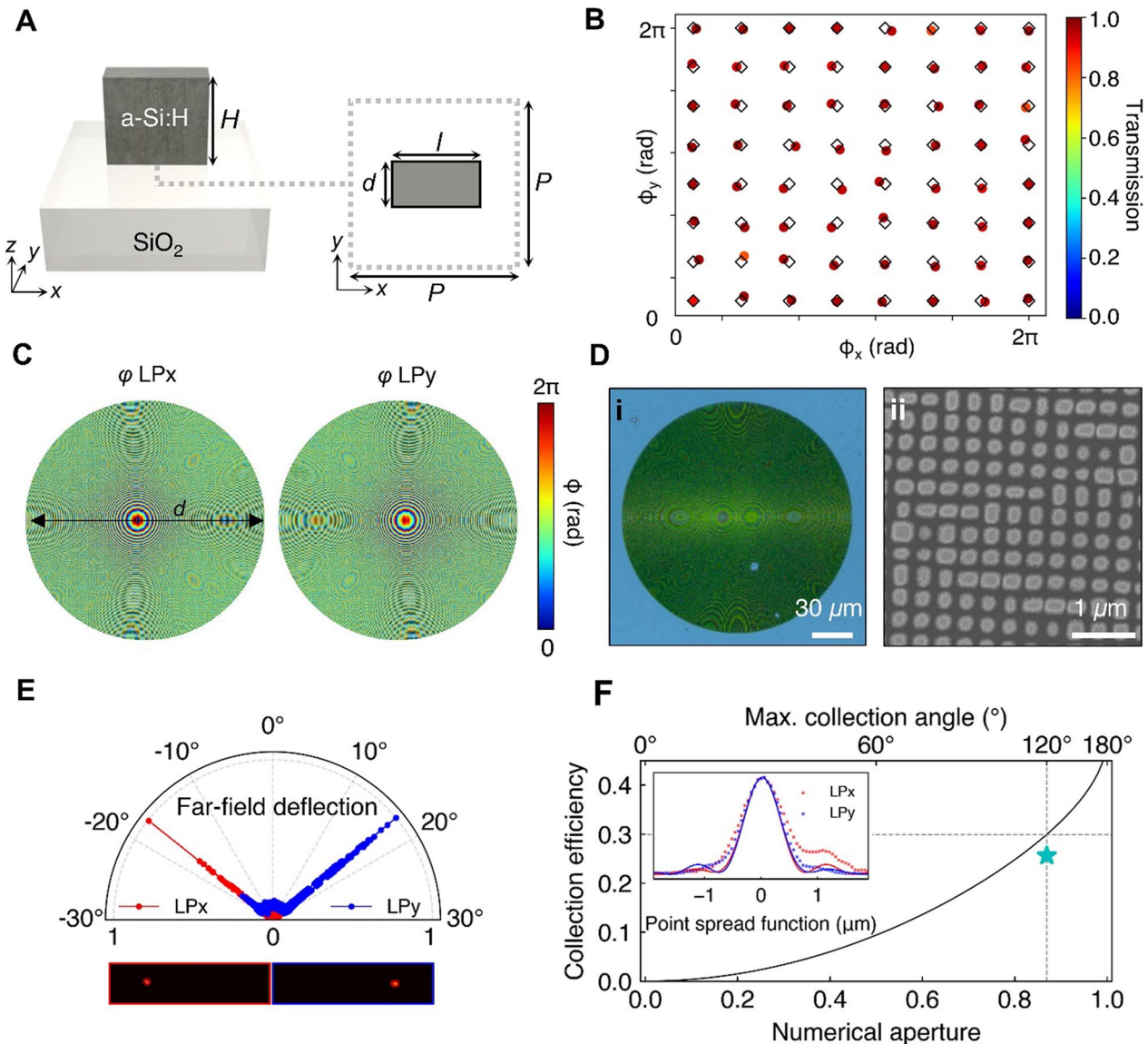


Fig. 2 Design and characterisation of a polarisation beam-splitting metalens. **A** Schematic of the meta-atoms made of low-loss a-Si:H on silica. **B** Calculated phase delay and transmission library of meta-atoms covering 2π for both LPx and LPy light. The average transmission is 94%. **C** Implemented phase maps for the metalens and gradient functions for LPx and LPy incidence. **D** Images of the fabricated metalens taken with an (i) optical microscope and (ii) scanning electron microscope. **E** Polar plot of the measured far-field deflection of the metalens under LPx and LPy dipole-like illumination. The bottom images are associated back-focal-plane image patterns. **F** Calculated collection efficiency of an isotropic emitter in free space as a function of numerical aperture of the collecting lens. A cyan star marks our metalens collection efficiency with $NA=0.869$. Inset: point spread function of the metalens under the LPx and LPy plane-wave incidence, where the scatter and solid lines represent the experimental and theoretical characterisations, respectively

solver. Eight phase steps between $0-2\pi$ are successfully achieved from various values of l and d at a fixed H of 550 nm (Fig. 2B). Any meta-atoms with a transmission lower than 80% were ruled out from the library, and the meta-atoms with the closest ϕ for both LP_x and LP_y were determined for each required phase step. The chosen 8×8 meta-atoms show an average transmission of 94%, and average discrepancy in ϕ of ~ 0.09 rad. The phase maps of a metalens with a high numerical aperture (NA) of 0.869 were designed to collect and collimate the emission from SPEs. To realise the control of directionality of LP_x and LP_y emissions, two independent linear phase gratings can be further implemented onto the lens profile of the orthogonal polarisations. The angle of the deflection depends on the grating period that the phase gradient cycles over 2π . As an example, the required phase maps for LP_x and LP_y to deflect beams in the $\pm x$ direction are shown in Fig. 2C, while the whole design process and lens functions are outlined in more detail in Additional file 1: Note S2.

To fabricate the designed metalens, we employ standard electron-beam lithography followed by a dry etching process (see Methods). Optical microscope as well as scanning electron microscope images of the metalens are shown in Fig. 2D. The cuboid shaped meta-atoms are fabricated with high accuracy across the metalens, albeit with a slightly slanted sidewall. We experimentally characterise the metalens performance through a dipole-like incidence (Additional file 1: Note S3). As shown in Fig. 2E, the fabricated metalens can efficiently deflect the orthogonal polarisations of LP_x and LP_y into different directions, with two distinct collimated beams propagating at around $\pm 16^\circ$. We define our metalens efficiency as the product of collection efficiency corresponding to the maximum collection angle (NA of the metalens) and total transmission efficiency of the metalens (Fig. 2F). The collection efficiency as a function of NA of an ideal lens with unity transmission efficiency in the air is shown in Fig. 2F [32]. Considering isotropic SPEs having the same radiation in all directions (i.e., uniform radiation), a high-NA lens of NA=0.869, corresponding to the maximum collection angle of 120° , leads to an ideal collection efficiency of 0.3. To experimentally verify the high NA of our metalens, we measure the point spread function (PSF) of the metalens based on an incident collimated beam (Additional file 1: Note S3). The cyan star marker in the figure denotes the fabricated metalens (NA of 0.869) collection efficiency, which considers both the average transmission efficiency of meta-atoms (~ 0.94) and the substrate transmittance (~ 0.91). Figure 2F inset shows the resulting PSF line profiles of the metalens in both experiment (scatter line) and theoretical calculation (solid line), showing a great agreement verifying that our

metalens has a high NA of 0.869. The small side lobes in the characterised PSF profiles are mainly due to the off-axis aberration in a tight focus [33].

2.2 Characterisation of quantum emission with a polarisation beam-splitting metalens

To prepare the hBN SPEs, the hBN solution containing SPEs is prepared on a glass substrate (see Methods). We choose SPEs with emission at ~ 610 nm, to match the designed metalens. First, the emitters are characterised using a conventional confocal microscope with a Hanbury Brown-Twiss interferometer to confirm the quantum nature of emitted light, as shown in Fig. 3A. Briefly, the hBN emitters are excited using a green (532 nm) laser and the emission is collected using same objective. The chosen SPE is shown in Fig. 3B, with a dominant zero-phonon line (ZPL) centred at 591 nm and a minor phonon sideband (PSB). Photon anti-bunching behaviour is confirmed by recording the second-order correlation function, $g^{(2)}(\tau)$, with a background corrected $g^{(2)}(0)=0.05$. Finally, the SPE dipole orientation is confirmed to be 106° (black arrow) with respect to the laboratory frame, as confirmed by rotating a linear polariser in the collection path (Fig. 3C).

We now utilise the metalens for multidimensional structuring of the quantum emission of the precharacterised hBN SPE. First, the metalens is used as a collection lens in the transmission path and the LP_x direction is set to horizontal (90°) as shown in Fig. 3C (red arrow). An SPE dipole-to-metalens LP_x intersection angle of 16° is hence derived. As expected, the SPE emission passes through the polarisation beam-splitting metalens and splits into LP_x (red curve) and LP_y (blue curve) as shown in Fig. 3D. Both photon streams result in sharp spectra with peaks centred at 591 nm, corresponding to the ZPL of the SPE. LP_x and LP_y polarisation are confirmed with a polariser and have been used to calibrate the metalens mounting angle. Note, the peak area ratio is $A_{\text{LP}_y}/A_{\text{LP}_x} = 0.19$ which is slightly higher than the anticipated dipole projection ratio $(\tan(16^\circ))^2 = 0.08$ in the orthogonal directions. One possible explanation is the variation of free space to fibre collection efficiency at each channel, as will be later confirmed by back-focal plane imaging. The inset in Fig. 3D shows confocal photoluminescence (PL) scans of the SPE as imaged through the metalens in both LP_x and LP_y channels, normalised to the LP_x maximum. The distinct emission from SPE as well as their signal-to-noise ratio are clearly visualised for each polarisation channel. The missing PSB peak is caused by the wavelength selectivity of the metalens, more discussion can be found in Additional file 1: Note S4.

To clarify that the detected photons are from the same SPE, 2nd order cross-correlation measurements between

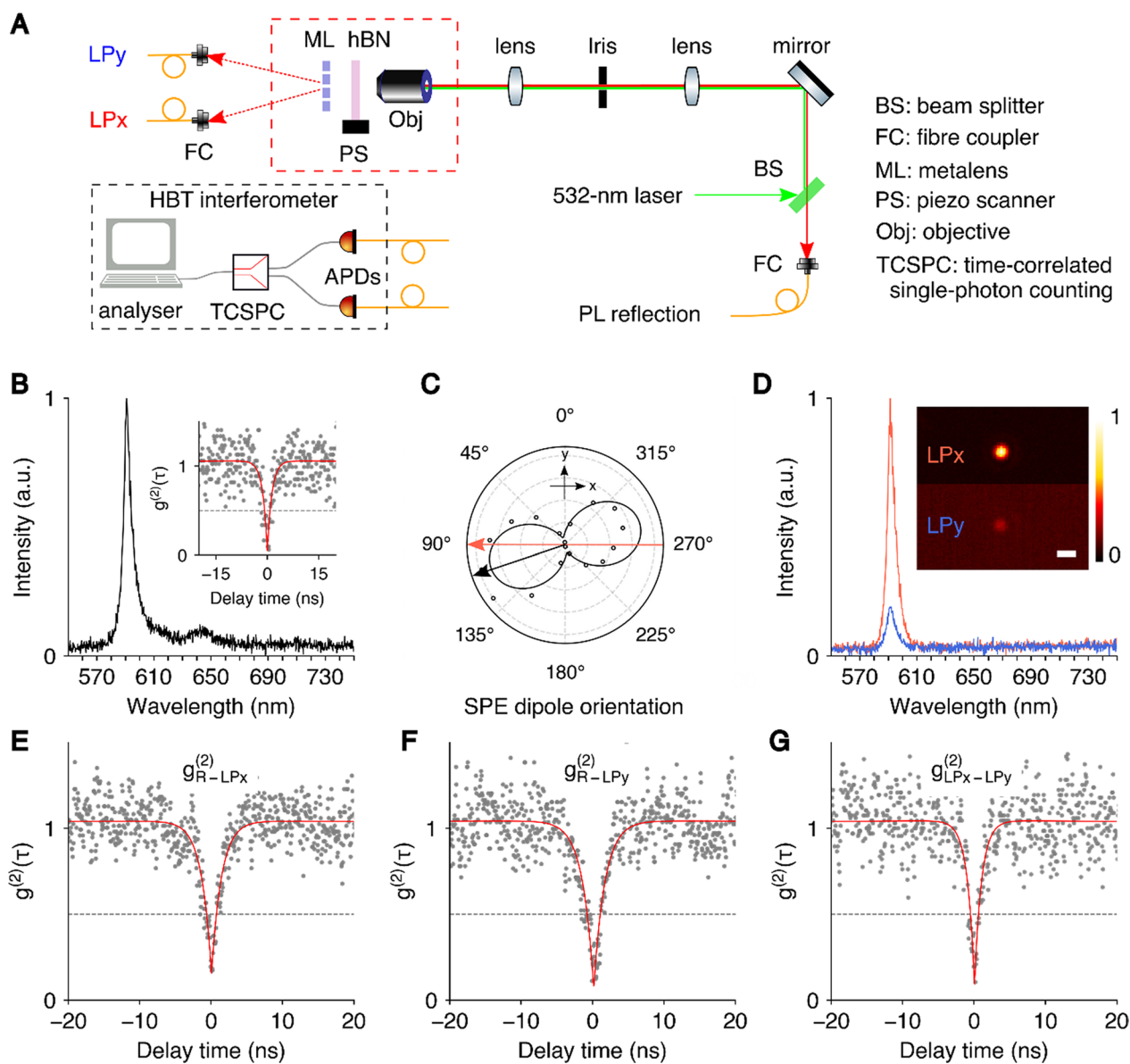


Fig. 3 Characterisation of hBN SPEs with the polarisation beam-splitting metalens. **A** A schematic optical setup for the photonic measurement. **B** PL collected via reflection channel (traditional objective) with a ZPL at ~591 nm. Inset, $g^{(2)}(\tau)$ confirmed the quantum nature of the SPE. **C** Emitter dipole orientation, measured from the reflection channel where 0° is the y (vertical) direction. The metalens orientation is set to 90° (red arrow). The emitter dipole orientation (black arrow) of 106° is derived after fitting with a sine function. **D** PL spectra collected from LPx (red curve) and LPy (blue curve) polarised channels employing the metalens. Insets are corresponding PL raster maps of the emitter. Colour bars in two maps are set to the same for a clear intensity contrast. Scale bars are 1 μm . **E–G** Cross correlation antibunching measurements from different channels. **E** Reflection PL and LPx correlation. **F** Reflection PL and LPy correlation. **G** LPx and LPy correlation. $g^{(2)}(\tau)$ data is background corrected

these PL channels are performed. Figure 3E and F show cross-correlation measurements between the emitter PL in reflection (employing a traditional objective) versus LPx and LPy (employing the metalens as the collecting lens). Figure 3G shows the cross-correlation between the two polarisation channels LPx and LPy (using the metalens to collect the light). Note that the correlation between LPx and LPy channels illustrates the

single-photon emission of the source. The same SPE with its corresponding quantum behaviour is verified across all three measurements, as all the $g^{(2)}(0)$ values approximately equal to 0.1 (Additional file 1: Note S5). These successful measurements confirm the potential of metalens for low-intensity light collection—as demonstrated with quantum emitters in hBN. Furthermore, the independent sample substrate enables its use as a confocal

mapping lens. To this extent, the results of other SPEs are shown in Additional file 1: Note S6.

2.3 Arbitrarily structuring quantum emission

After confirming the beam-splitting metalens efficiently collects and spatially separates the linear polarisation

streams of the emitted light from SPEs, we imprint different functionalities on the metalenses for multi-dimensional structuring of quantum emission. We design and fabricate four different metalenses with distinct functionalities and increasing complexity, as shown schematically in Fig. 4A. By employing the 8-step (16-step)

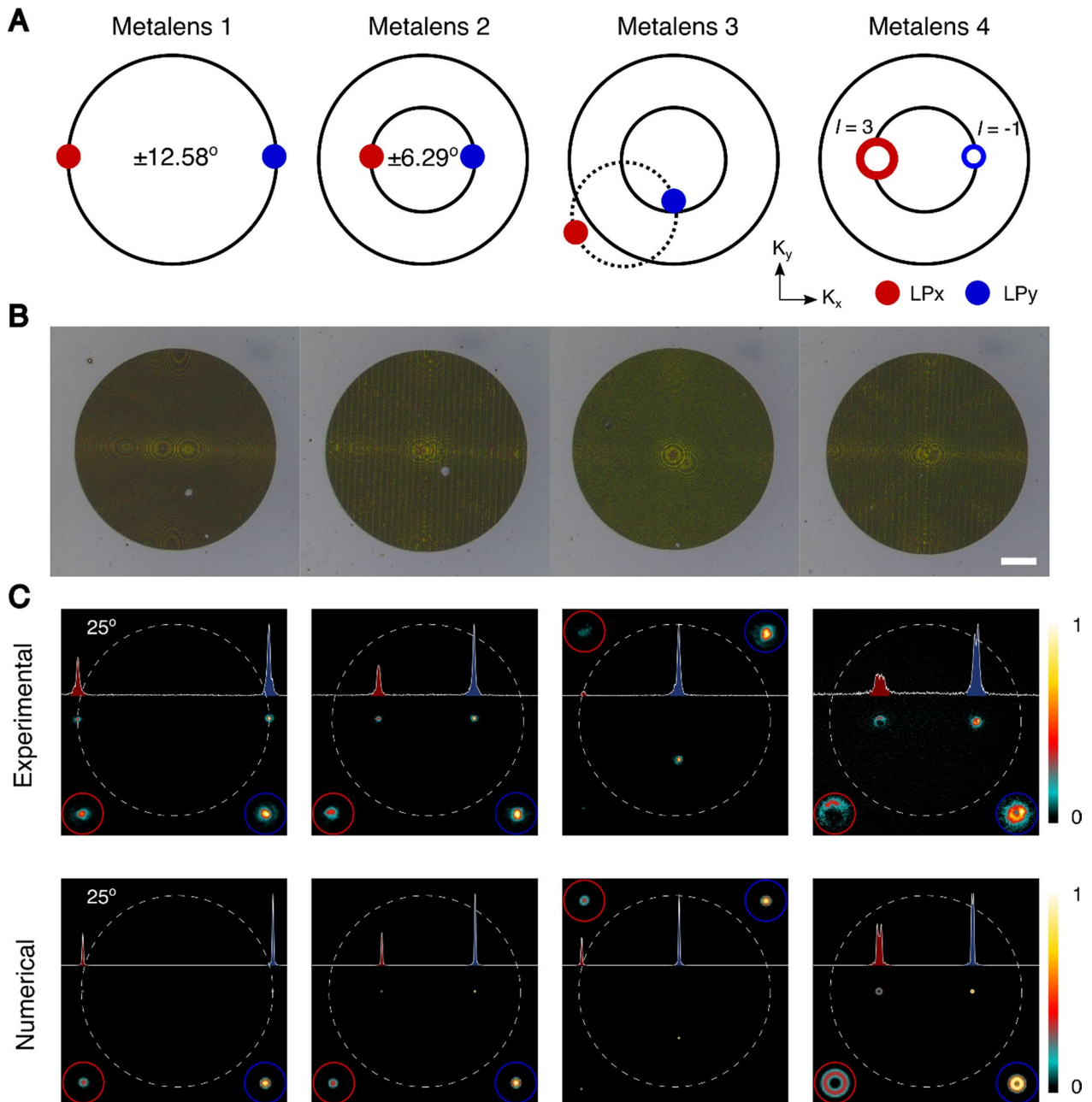


Fig. 4 Arbitrary structured quantum emission with polarising beam-splitting metalenses. **A** Schematics of different metalens functionalities. The circles represent desired positions for orthogonal linear polarisations in the K space. The doughnut-shaped spots indicate the generation of OAM. **B** Far-field optical images of the fabricated metalenses. Scale bar is 30 μm . **C** Experimental (top) and numerically calculated (bottom) results of the SPE far-field back focal imaging. Curves in c represent the vertically accumulated PL intensity of the LPx (filled with red) and LPy (filled with blue). The red and blue circles are zoomed-in insets for highlighting the intensity distributions of the orthogonal polarisations

phase meta-atoms, Metalens 1(2) deflects LP_x and LP_y to angles of $\pm 12.58^\circ$ ($\pm 6.29^\circ$) along the x-direction, respectively. Metalens 3 deflects LP_x and LP_y in arbitrary directions, shifted from the centre, and finally, Metalens 4 encodes different helical phase fronts carrying distinctive OAM values ($l=3$ and $l=-1$, in our case)—in addition to the directionality and polarisation. Figure 4B shows the far-field optical images of the fabricated four metalenses and their characteristic interference patterns. We then employ these metalenses to image the same SPE, as presented in Fig. 3.

The results of the four metalenses are shown in Fig. 4C. For convenience and clarity, we rotate the emitter to 146° , resulting in a dipole-to-metalens intersection angle of 56° , to balance the emission rates of the two channels (Additional file 1: Note S7). The white dash circles in the images represent the maximum splitting angle of 25° , while the inset red (blue) circle is a zoomed-in image of the LP_x (LP_y) spot. Using Metalens 1 we observe two bright spots, and the PL signals (summed in Ky direction) gave a clear peak profile of the two spots with an intensity ratio of $A_{LP_y}/A_{LP_x} = 1.8$, indicating a dipole projection angle of 53° which aligns well with the measured 56° . Metalens 2 demonstrates axial symmetric deflection with a half-splitting angle compared to Metalens 1. As expected, the emitters are imaged closer, with a smaller deflection angle and spot intensity ratio of $A_{LP_y}/A_{LP_x} = 1.8$. Metalens 3 splits the incoming SPE asymmetrically, with two spots falling into the same side and also deflected in the y axis ($A_{LP_y}/A_{LP_x} = 13.7$). The combination of Metalenses 1–3 hence allows for complete direction and polarisation control of the imaged SPEs. As a final demonstration, we employ Metalens 4 to show two doughnut beams (zoomed-in in the insets) that correspond to the OAM with topological charges of $l=3$ and $l=-1$ for the LP_x and LP_y channels, respectively. Since the larger OAM leads to larger doughnut intensity distribution in the momentum space, LP_y becomes brighter than LP_x ($A_{LP_y}/A_{LP_x} = 2.0$). Furthermore, we experimentally confirm that the two structured beams carry the correct topological charges (Additional file 1: Note S8). Moreover, structuring SPE with the OAM property is achieved from the phase manipulation, which conserves the sub-Poissonian photon statistics and does not affect the antibunching nature of the photons. As a result, our metalens conclusively demonstrates a complete control of single photons in directionality, polarisation and OAM dimensions, simultaneously.

To support these results, we have also performed scalar wave propagation calculations. Complex-amplitude profiles were extracted from the four metalens with two polarisation channels, then modified by assuming the dipole source is located at the exact focal position

(subtraction of lens phase in each profile). First, each modified profile with the two polarisation channels was used to evaluate far-field profiles using Rayleigh-Sommerfeld (RSD) diffraction integral. Then, far-field images in the LP_x and LP_y channel were directly integrated by considering the polarisation angle of the dipole source (Fig. 4C bottom panel). Each metalens performs the desired function well, showing a clear collimated beam that is successfully structured as designed. Compared to previous demonstrations [23–25], this work presents for the first time multi-dimensional shaping of quantum emission by using a single metalens structure, capable of simultaneous control of the linear momentum, polarisation, and OAM of SPEs (Additional file 1: Table S1).

3 Discussion

In this work, we proposed and implemented a multi-functional metalens to arbitrarily structure quantum light sources at room temperature. Realised with bright and linearly polarised SPEs in hBN, our designed and fabricated polarisation beam-splitting metalens allows independent wavefront shaping of orthogonal linear polarisations. We further experimentally demonstrated arbitrary directionality control of single photon emission, as well as imprinting different OAM modes onto its orthogonal polarisations. As such, our demonstration offers a new platform to use ultrathin meta-optics for arbitrary wavefront shaping of quantum emission in multiple degrees of freedom at room temperature. It may provide new insights into the field of quantum information science—specifically manipulating photon polarisations has great impact for quantum cryptography and entanglement distribution with improved filtering. The polarisation separation is vital, for future employment of hBN SPEs for polarisation entangled photon pair generation, as it is commonly used for down converted photon sources [34]. Notably, a major reason of choosing SPE instead of other types of point-like sources is because manipulating quantum source instead of classic photoluminescence meets the needs of quantum photonics. For future quantum applications, we will need not only abundant quantum sources with various on-demand properties but also miniaturised device footprint for good scalability. To the best of our knowledge, this work has achieved the highest degrees of freedom in the manipulation of SPEs in the air environment at a room temperature.

Although the focus here is the multi-functionality and flexibility of the metalens to image a selected SPE, integration of hBN SPE to metalens could also be possible by bulk engineering or addition of a transparent spacer [35], adapting device architectures and aligning approaches developed earlier [26]. Photon collection of solid-state

SPEs is an outstanding challenge which may hinder practical applications. Indeed, various strategies to enhance photon collection have been demonstrated, including the use of distributed Bragg reflectors [36], perturbed photonic crystal cavities [37], circular grating cavities [38, 39], nano-antennas [40], and solid immersion lenses [25]. We believe their implementation with our demonstrated wavefront-shaping metasurface is not a trivial task and beyond the scope of current work, where we focus on improving functionality, rather than focusing solely on collection enhancement. We note, that our proposed hybrid hBN—silica metalens can be implemented together with any additional photon collector.

Moreover, our confocal mapping metalens endows a direct access to the OAM states of single photons, offering a compact platform for high-dimensional quantum entanglement to increase the quantum information capacity [41–44]. Future extension of the metalens to realise higher-order structured vector beams [41, 45, 46] could enable the generation of high-dimensional single-photon hybrid quantum states. Furthermore, future integration of structured SPE sources with a reliable transmission environment such as optical fibres [47] could promise a quantum network with higher information capacity, robustness to noise and better security. Lastly, we envision that combining the spin defects in hBN with the proposed multifunctional metalens may enable efficient spin photon readout and remote quantum sensing [48–52].

4 Methods

4.1 Numerical calculations

The propagation phase delay and field profiles of the meta-atoms were calculated using an in-house built RCWA solver. The far-field propagation of the four metalenses was calculated using scalar diffraction, specifically the RSD integral method. The input amplitude and phase profiles for each metalens were retrieved from the S parameters of the spatially arranged meta-atoms.

4.2 Sample preparation

4.2.1 Metalens fabrication

Plasma-enhanced chemical vapour deposition (PECVD, BMR Technology HiDEP-SC) was used to deposit a 550-nm-thick hydrogenated amorphous silicon (a-Si:H) layer on a 500- μm -thick silica wafer. A gas flow rate, chamber pressure and operating temperature were set to be 10 sccm for SiH_4 and 75 sccm for H_2 , 25 mTorr, and 200 °C, respectively. The standard electron-beam lithography process (ELIONIX, ELS-7800) was used to transfer the designed metalens onto the positive photoresist (495 PMMA A6, Micro-Chem). The acceleration voltage and beam current were set to be 80 kV and 500 pA,

respectively. The exposed photoresist patterns were developed in methyl isobutyl ketone/IPA (1:3) solution for 10 min at 0 °C. The electron-beam evaporation (KVT, KVE-KVE-ENS4004) was used to deposit a 60-nm-thick chromium (Cr) mask and residual unexposed photoresists were stripped using acetone. The Cr mask pattern was transferred onto the a-Si:H layer using dry etching (DRM85DD, TEL). The residual Cr mask was removed using Cr etchant (CR-7).

4.2.2 hBN sample preparation

hBN nanoflake solution (few layers with submicrometer lateral size, Graphene Supermarket) was drop casted on a gold-marked thin glass coverslip, and then dried on a hotplate at 50 °C for 5 min, followed by 400 °C annealing on a hotplate for 3 h and 5 min UV ozone plasma to oxidise the potential organic residuals. SPEs within the target spectral range (610 ± 20 nm) were then pre checked by a lab-built confocal microscope and later relocated with the assistance of gold markers. For the specific sample used in this work, we can roughly find less than ten emitters per scan ($50 \times 50 \mu\text{m}^2$).

4.3 Experimental setup

4.3.1 Metalens characterisation

The schematics of the optical setups for metalens characterisation are illustrated in Additional file 1: Note S3. A continuous-wave laser beam at 633 nm (CPS635, Thorlabs) was first passed through a spatial filter system which consists of two concave lenses and a 5 μm pinhole (P5CB, Thorlabs). Then the beam was linearly polarised using a linear polariser (LPVISE100-A, Thorlabs), and the polarisation angle was tuned using a halfwave plate (AHWP10M-600, Thorlabs). For PSF imaging, a weakly focused beam using a $4\times/0.13$ NA objective (LMPlanFL N, Olympus) was incident on the metalens. The focused beam by the metalens was captured using an imaging setup comprised of a $100\times/0.8$ NA objective (LMPlanFL N, Olympus), tube lens (TTL180-A, Thorlabs), and CCD (INFINITY2-1RC, Infinity). For imaging far-field patterns, the beam was tightly focused by the $100\times/0.8$ NA objective to imitate dipole emission. The dipole-like beam was then collected and collimated by the metalens. A back focal image of the collimated beam was formed at the back focal plane using a $20\times/0.45$ NA objective (LMPlanFL N, Olympus), and captured using two concave lenses and sCMOS camera (Panda 4.2 bi UV, PCO).

4.3.2 SPE-metalens PL characterisation

The schematics of a lab-built optical setup for SPE-metalens characterisation are illustrated in Fig. 3A. A 532-nm CW laser (Gem 532TM, Laser Quantum Ltd.) was used to pump the SPE through a $100\times/0.9\text{NA}$ air

objective (TU Plan Fluor, Nikon), reflected PL signal was filtered by a beam splitter and long pass filter before being coupled into a 62.5- μm core multimode fibre and then connected to a spectrometer (Princeton Instruments, Inc.). Or be split by a 50:50 fibre splitter and went into two avalanche photodiodes (APDs, SPCM-AQRH-16, Excelitas Technologies) for Hanbury Brown and Twiss measurements. The transmission PL was collected by the metalens. Given the short focal distance of the metalens, the hBN side and metalens side were placed face to face. Next, the metalens location was first confirmed by the supercontinuum white light laser (SuperK Fianium, NKT) with the wavelength being set to the same wavelength of the emitter. Two collimated beam spots can be observed once the metalens focal plane reaches the focal spot of the incoming laser. The sample mounting and aligning platform are shown in Additional file 1: Note S7. The two beams were then independently coupled into two multimode fibres (core size 62.5 μm) and then can be connected either to a spectrometer or an APD. Photon correlation was done by a time-correlated single-photon counting module (PicoHarp 300, PicoQuant). All measurements were done under an excitation power of 500 μW (before objective). And 568-nm long pass filters are used to filter out lasers in all collections.

4.3.3 SPE-metalens back focal imaging characterisation

Back-focal plane imaging allows the direct measurement of the far-field intensity distribution emanating from the single-photon source. The optical setup used is similar to the metalens characterisation setup (Additional file 1: Note S3), where a back focal image of the collimated beam is formed at the back focal plane using a 20 \times /0.4 NA objective (LMPlanFL N, Olympus). Then acquired by an EMCCD (iXon Ultra 888) placed at a distance of $4f$ away from the objective on a path, separate from the main confocal collection pathway.

Supplementary Information

The online version contains supplementary material available at <https://doi.org/10.1186/s43593-023-00052-4>.

Additional file 1: Note S1. Measured refractive index of a-Si:H. **Note S2.** Metalens design and function. **Note S3.** Metalens characterisation setups. **Note S4.** Wavelength selectivity. **Note S5.** g background correction. **Note S6.** Additional SPEs coupled to the metalens. **Note S7.** Far-field back focal imaging. **Note S8:** OAM modes characterisation. **Table S1.** Comparison of this work with the state-of-the-art metalens for multi-dimensional quantum emission control.

Acknowledgements

The authors thank Milos Toth, Yongliang Chen and Simon White for their fruitful discussion. This work was performed in part at the Melbourne Centre for

Nanofabrication (MCN), the Victorian Node of the Australian National Fabrication Facility (ANFF).

Author contributions

IA, HR, and JR conceived the concept of this project. CL prepared SPEs and conducted the SPE-metalens measurements. JJ conducted optical characterisation of the metalenses. TB and JJ designed the metalenses. JHK and JKK fabricated the metalenses. CL, TY and MN built the photonic characterisation platform for the SPE-metalens system. CL, JJ, TB, S.A.M. and H.R. analysed the data. All authors discussed the results and wrote the manuscript.

Funding

This work was supported by Australian Research Council (CE200100010, DE220101085, DP220102152) and the Office of Naval Research Global (N62909-22-1-2028) (I.A.). S.A.M. acknowledges the Lee-Lucas Chair in Physics. J.R. acknowledges the POSCO-POSTECH-RIST Convergence Research Center program funded by POSCO, the Basic Science grant (SSTF-BA2102-05) funded by the Samsung Science and Technology Foundation, and the National Research Foundation (NRF) grant (NRF-2022M3C1A3081312) funded by the Ministry of Science and ICT (MSIT) of the Korean government. J.J. acknowledges the NRF Sejong Science fellowship (NRF-RS-2023-00209560) funded by the MSIT of Korea government. T.B. acknowledges the Institute of Information & Communications Technology Planning & Evaluation (IITP) grant (No. 2019-0-01906, the POSTECH Artificial Intelligence Graduate School program) funded by the MSIT of the Korean government, and the POSTECH PIURI fellowship. J.H.K. acknowledges the POSTECH Alchemist fellowship.

Availability of data and materials

The main data supporting the findings of this study are available within the article and its Additional information files. Extra data are available from the corresponding author upon reasonable request.

Declarations

Competing interests

Igor Aharonovich serves as an Editor for the Journal, no other author has reported any competing interests.

Received: 22 April 2023 Revised: 27 May 2023 Accepted: 12 June 2023
Published online: 07 August 2023

References

- D.D. Awschalom, R. Hanson, J. Wrachtrup, B.B. Zhou, Quantum technologies with optically interfaced solid-state spins. *Nat. Photonics* **12**, 516–527 (2018)
- X. Liu, M.C. Hersam, 2D materials for quantum information science. *Nat. Rev. Mater* **4**, 669–684 (2019)
- I. Aharonovich, J.P. Tetienne, M. Toth, Quantum emitters in hexagonal boron nitride. *Nano Lett* **22**, 9227–9235 (2022)
- J.D. Caldwell et al., Photonics with hexagonal boron nitride. *Nat. Rev. Mater* **4**, 552–567 (2019)
- F. Hayee et al., Revealing multiple classes of stable quantum emitters in hexagonal boron nitride with correlated optical and electron microscopy. *Nat. Mater* **19**, 534–539 (2020)
- P. Senellart, G. Solomon, A. White, High-performance semiconductor quantum-dot single-photon sources. *Nat. Nanotechnol.* **12**, 1026–1039 (2017)
- A.H. Dorrah, F. Capasso, Tunable structured light with flat optics. *Science* **376**, eabi6860 (2022)
- M.L. Tseng et al., Vacuum ultraviolet nonlinear metalens. *Sci. Adv.* **8**, eabn5644 (2022)
- T. Santiago-Cruz et al., Resonant metasurfaces for generating complex quantum states. *Science* **377**, 991–995 (2022)
- A.S. Solntsev, G.S. Agarwal, Y.S. Kivshar, Metasurfaces for quantum photonics. *Nat. Photonics* **15**, 327–336 (2021)
- J. Ni et al., Multidimensional phase singularities in nanophotonics. *Science* **374**, eabj0039 (2021)

12. L. Li et al., Metalens-array-based high-dimensional and multiphoton quantum source. *Science*. **368**, 1487–1490 (2020)
13. K. Wang et al., Quantum metasurface for multiphoton interference and state reconstruction. *Science*. **361**, 1104–1108 (2018)
14. H. Ren et al., An achromatic metafiber for focusing and imaging across the entire telecommunication range. *Nat. Commun.* **13**, 4183 (2022)
15. T. Badloe, I. Kim, Y. Kim, J. Kim, J. Rho, Electrically tunable Bifocal Metalens with Diffraction-Limited focusing and imaging at visible wavelengths. *Adv. Sci.* **8**, e2102646 (2021)
16. W.J. Joo et al., Metasurface-driven OLED displays beyond 10,000 pixels per inch. *Science*. **370**, 459–463 (2020)
17. X. Ni, A.V. Kildishev, V.M. Shalaev, Metasurface holograms for visible light. *Nat. Commun.* **4**, 1–6 (2013)
18. H. Ren et al., Complex-amplitude metasurface-based orbital angular momentum holography in momentum space. *Nat. Nanotechnol.* **15**, 948–955 (2020)
19. L. Jin et al., Dielectric multi-momentum meta-transformer in the visible. *Nat. Commun.* **10**, 4789 (2019)
20. X. Fang, H. Ren, M. Gu, Orbital angular momentum holography for high-security encryption. *Nat. Photonics*. **14**, 102–108 (2020)
21. S. So et al., Multicolor and 3D Holography generated by inverse-designed single-cell metasurfaces. *Adv. Mater.* **35**, 2208520 (2023)
22. S.Q. Li et al., Phase-only transmissive spatial light modulator based on tunable dielectric metasurface. *Science*. **364**, 1087–1090 (2019)
23. I. Kim et al., Holographic metasurface gas sensors for instantaneous visual alarms. *Sci. Adv.* **7**, eabe9943 (2021)
24. F. Yang, P.K. Jha, H. Akbari, H.C. Bauser, H.A. Atwater, A hybrid coupler for directing quantum light emission with high radiative Purcell enhancement to a dielectric metasurface lens. *J. Appl. Phys.* **130**, 163103 (2021)
25. T.Y. Huang et al., A monolithic immersion metalens for imaging solid-state quantum emitters. *Nat. Commun.* **10**, 2392 (2019)
26. Y. Bao et al., On-demand spin-state manipulation of single-photon emission from quantum dot integrated with metasurface. *Sci. Adv.* **6**, eaba8761 (2020)
27. C. Wu et al., Room-temperature on-chip orbital angular momentum single-photon sources. *Sci. Adv.* **8**, eabk3075 (2022)
28. E.N. Knall et al., Efficient source of shaped single photons based on an Integrated Diamond Nanophotonic System. *Phys. Rev. Lett.* **129**, 053603 (2022)
29. B. Chen et al., Bright solid-state sources for single photons with orbital angular momentum. *Nat. Nanotechnol.* **16**, 302–307 (2021)
30. Y. Yang et al., Revealing Structural Disorder in Hydrogenated Amorphous Silicon for a low-loss Photonic platform at visible frequencies. *Adv. Mater.* **33**, e2005893 (2021)
31. G. Yoon, K. Kim, D. Huh, H. Lee, J. Rho, Single-step manufacturing of hierarchical dielectric metalens in the visible. *Nat. Commun.* **11**, 2268 (2020)
32. W. Barnes et al., Solid-state single photon sources: light collection strategies. *Eur. Phys. J. D-Atomic Mol. Opt. Plasma Phys.* **18**, 197–210 (2002)
33. Y. Guo et al., High-efficiency and wide-angle beam steering based on catenary optical fields in ultrathin metalens. *Adv. Opt. Mater.* **6**, 1800592 (2018)
34. P.G. Kwiat et al., New high-intensity source of polarization-entangled photon pairs. *Phys. Rev. Lett.* **75**, 4337–4341 (1995)
35. J.L. O'Brien, A. Furusawa, J. Vučković, Photonic quantum technologies. *Nat. Photonics*. **3**, 687–695 (2009)
36. F. Basso Basset et al., Quantum key distribution with entangled photons generated on demand by a quantum dot. *Sci. Adv.* **7**, eabe6379 (2021)
37. M. Toishi, D. Englund, A. Faraon, J. Vuckovic, High-brightness single photon source from a quantum dot in a directional-emission nanocavity. *Opt. Express*. **17**, 14618–14626 (2009)
38. J.E. Froch et al., Coupling spin defects in hexagonal boron nitride to monolithic bullseye cavities. *Nano Lett* **21**, 6549–6555 (2021)
39. J. Liu et al., A solid-state source of strongly entangled photon pairs with high brightness and indistinguishability. *Nat. Nanotechnol.* **14**, 586–593 (2019)
40. X.-L. Chu et al., Experimental realization of an optical antenna designed for collecting 99% of photons from a quantum emitter. *Optica*. **1**, 203–208 (2014)
41. A. Mair, A. Vaziri, G. Weihs, A. Zeilinger, Entanglement of the orbital angular momentum states of photons. *Nature*. **412**, 313–316 (2001)
42. R. Fickler et al., Quantum entanglement of high angular momenta. *Science*. **338**, 640–643 (2012)
43. M. Malik et al., Multi-photon entanglement in high dimensions. *Nat. Photonics*. **10**, 248–252 (2016)
44. T. Badloe, S. Lee, J. Rho, Computation at the speed of light: metamaterials for all-optical calculations and neural networks. *Adv. Photonics*. **4**, 064002 (2022)
45. A. Forbes, M. de Oliveira, M.R. Dennis, Structured light. *Nat. Photonics*. **15**, 253–262 (2021)
46. T. Stav et al., Quantum entanglement of the spin and orbital angular momentum of photons using metamaterials. *Science*. **361**, 1101–1104 (2018)
47. D. Cozzolino et al., Orbital angular momentum states enabling fiber-based high-dimensional quantum communication. *Phys. Rev. Appl* **11**, 064058 (2019)
48. A. Gottscholl et al., Spin defects in hBN as promising temperature, pressure and magnetic field quantum sensors. *Nat. Commun.* **12**, 4480 (2021)
49. H.L. Stern et al., Room-temperature optically detected magnetic resonance of single defects in hexagonal boron nitride. *Nat. Commun.* **13**, 618 (2022)
50. N. Chejanovsky et al., Single-spin resonance in a van der Waals embedded paramagnetic defect. *Nat. Mater.* **20**, 1079–1084 (2021)
51. X. Gao et al., Nuclear spin polarization and control in hexagonal boron nitride. *Nat. Mater.* **21**, 1024–1028 (2022)
52. I.O. Robertson et al., Imaging current control of magnetization in Fe₃GeTe₂ with a widefield nitrogen-vacancy microscope. *2D Mater.* **10**, 015023 (2022)